

Aerial-ground Cross-modal Localization: Dataset, Ground-truth, and Benchmark

Yandi Yang^a, Jianping Li^{b,*}, Youqi Liao^c, Yuhao Li^d, Yizhe Zhang^c, Zhen Dong^c, Bisheng Yang^c and Naser El-Sheimy^a

^aDepartment of Geomatics Engineering, University of Calgary, Calgary, T2N 1N4, Canada

^bSchool of Electrical and Electronic Engineering, Nanyang Technological University, 639798, Singapore

^cState Key Laboratory of Information Engineering in Surveying, Mapping and Remote Sensing, Wuhan University, Wuhan, 430079, China

^dSchool of Mechanical Engineering, Chongqing Technology and Business University, Chongqing, 400067, China

ARTICLE INFO

Keywords:

Localization
Navigation
Cross-modal fusion
Airborne Laser Scanning (ALS)
LiDAR

ABSTRACT

Accurate visual localization in dense urban environments poses a fundamental task in photogrammetry, geospatial information science, and robotics. While imagery is a low-cost and widely accessible sensing modality, its effectiveness on visual odometry is often limited by textureless surfaces, severe viewpoint changes, and long-term drift. The growing public availability of airborne laser scanning (ALS) data opens new avenues for scalable and precise visual localization by leveraging ALS as a prior map. However, the potential of ALS-based localization remains underexplored due to three key limitations: (1) the lack of platform-diverse datasets, (2) the absence of reliable ground-truth generation methods applicable to large-scale urban environments, and (3) limited validation of existing Image-to-Point Cloud (I2P) algorithms under aerial-ground cross-platform settings. To overcome these challenges, we introduce a new large-scale dataset that integrates ground-level imagery from mobile mapping systems with ALS point clouds collected in Wuhan, Hong Kong, and San Francisco. Accurate 6-DoF ground-truth poses for the images are obtained indirectly, by first aligning mobile LiDAR scans (MLS) with ALS data through ground segmentation, façade reconstruction, and multi-sensor pose graph optimization. Given the rigid mounting between LiDAR and camera, the optimized MLS trajectory is then transferred to the image stream, enabling reliable image-ALS localization. This strategy circumvents the difficulty of direct cross-modal registration and provides a robust basis for benchmarking. Finally, we evaluate state-of-the-art global and fine I2P localization methods under cross-view and cross-modal conditions. Our dataset and benchmarks aim to facilitate research in air-ground localization, multi-source data fusion, and urban-scale photogrammetric applications. The project page is available at: https://yandiyang.github.io/aerial_ground_cross_modal/.

1. Introduction

Accurate localization in urban environments is a core task in photogrammetry, geospatial information science, and robotics, underpinning a wide range of applications such as urban mobile mapping (Schwarz and El-Sheimy, 2004), autonomous navigation (El-Sheimy and Youssef, 2020), and robotic delivery (Li et al., 2024b, 2025a). In densely built-up areas, Global Navigation Satellite System (GNSS) signals are often severely degraded or entirely unavailable due to signal occlusion and multipath effects caused by tall structures and narrow streets (Nassar and El-Sheimy, 2006). Although Inertial Navigation Systems (INSs) can maintain short-term localization continuity, they suffer from cumulative drift in the absence of reliable external corrections (El-Sheimy and Youssef, 2020). Among various sensing modalities, consumer-grade cameras have become the most ubiquitous due to their low cost, compact form factor, and widespread integration across mobile platforms, including smartphones, vehicles, and autonomous systems.

As a passive, power-efficient, and semantically rich sensing modality, imagery has strong potential for scalable localization in complex urban scenes with prebuilt reference maps, such as point clouds (Li et al., 2025b; Zou et al., 2025; Liao et al., 2024b), ground view images (Warburg et al., 2020), airborne images (Jende et al., 2018), and OpenStreetMap (OSM) (Liao et al., 2024a).

Visual localization using pre-built maps in highly urbanized environments remains a challenging task. Although numerous visual place recognition algorithms have been proposed, most existing ground-view image references, such as those from Mapillary, are collected non-uniformly by tourists or ground vehicles, resulting in sparse and uneven spatial coverage (Warburg et al., 2020). Relocalization based on 2D reference maps, including satellite imagery and OpenStreetMap (OSM), is limited to 3-DoF pose estimation with restricted accuracy, despite their broad accessibility and ease of use (Liao et al., 2024a; Sarlin et al., 2023a,b). In contrast, 6-DoF localization can be achieved using 3D pre-built maps such as point clouds and meshes, offering improved geometric fidelity. Furthermore, the growing public availability (CEDD, Hong Kong, 2020; USGS, U.S.A., 2023) of Airborne Laser Scanning (ALS) point clouds from governmental agencies worldwide presents new opportunities for scalable and accurate 6-DoF visual localization using ALS as a prior map.

* This research was supported by the National Natural Science Foundation Project (No. 42201477, No.42130105)

*Corresponding author

✉ yandi.yang@ucalgary.ca (Y. Yang); jianping.li@ntu.edu.sg (J. Li); martin_liao@whu.edu.cn (Y. Liao); yhaoli@whu.edu.cn (Y. Li); yizhezhang0418@whu.edu.cn (Y. Zhang); dongzhenwhu@whu.edu.cn (Z. Dong); bshyang@whu.edu.cn (B. Yang); elsheimy@ucalgary.ca (N. El-Sheimy)

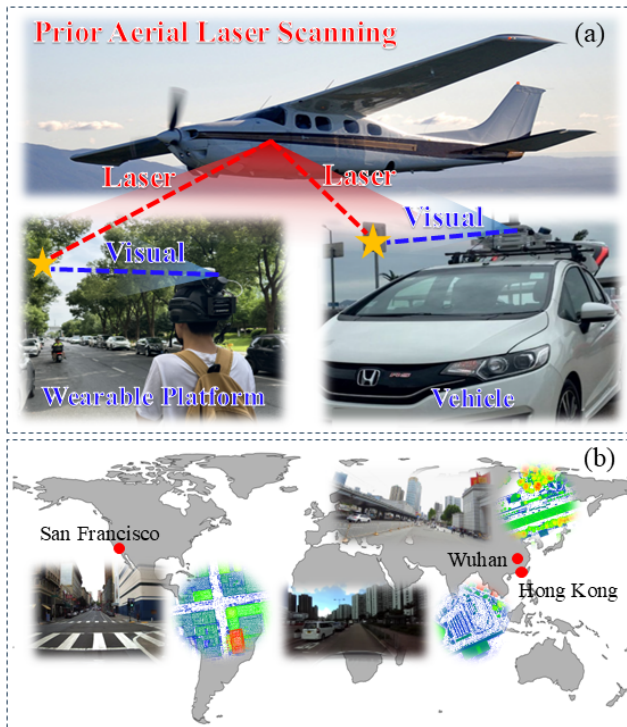


Fig. 1. Global distribution of our dataset on the map.

Despite its potential, ALS-based visual localization in urban environments remains underexplored due to three major challenges. First, most publicly available datasets lack platform diversity, particularly the integration of both ground and aerial sensing platforms. To date, there is no dataset specifically designed to support image-based localization using ALS data in urban contexts. Second, ground-truth trajectories are often obtained through loop closure techniques or depend on external reference systems such as high-end IMUs (Li et al., 2023a). However, these approaches become unreliable or impractical for ground-based platforms operating in large-scale urban environments (El-Sheimy and Youssef, 2020). Third, existing Image-to-Point Cloud (I2P) methods are predominantly developed for ground-platform scenarios (Li et al., 2025b), limiting their generalizability across aerial and ground platforms.

The above challenges underscore the need for a comprehensive benchmark that facilitates rigorous evaluation of cross-view and cross-modal localization methods. To address these issues, we propose an air-ground cross-modal localization dataset. The main contributions of this article are as follows.

- 1) We present a new large-scale dataset that enables aerial-ground cross-modal localization by combining ground-level imagery from mobile mapping systems with ALS point clouds. The data span three representative urban areas—Wuhan, Hong Kong, and San Francisco—and will be made publicly accessible to the research community.
- 2) We propose an indirect yet scalable approach for generating accurate 6-DoF ground-truth image poses. This is

achieved by registering mobile LiDAR submaps to ALS data using ground segmentation and façade reconstruction, followed by multi-sensor pose graph optimization.

- 3) We establish a unified benchmarking suite for both global and fine-grained I2P localization, and evaluate state-of-the-art methods under challenging cross-view and cross-modality conditions. Future research trends are summarized according to the evaluation results.

The remainder of this paper is organized as follows. Section 2 reviews existing algorithms and datasets related to cross-view and cross-modal localization, along with methods for generating ground-truth trajectories. Section 3 details the composition and characteristics of the proposed dataset. Section 4 describes the methodology for ground-truth trajectory generation, while Section 5 presents its qualitative and quantitative evaluation. Section 6 benchmarks state-of-the-art Image-to-Point Cloud (I2P) localization algorithms under aerial-ground cross-modal settings. Section 7 discusses the remaining challenges in air-ground cross-modal localization. Finally, conclusions are drawn in Section 8.

2. Related work

2.1. Cross-platform localization and dataset

2D maps, such as satellite images (Ye et al., 2024) and OpenStreetMap (Wu et al., 2024), have been widely used for visual localization due to their extensive coverage and accessibility. However, they are restricted to estimating 3-DoF poses with limited accuracy. Various forms of 3D maps can also be used to enhance localization accuracy, with point clouds (Zhang et al., 2023) being a widely adopted choice. However, acquiring prior point cloud maps is often costly and time-consuming, which limits their broad applicability. A similar challenge arises with methods that rely on 3D line maps (Liu et al., 2024), 3D meshes (Merat et al., 2024), CAD models (Aubry et al., 2014), and HD maps (Jeong et al., 2024), as data acquisition also demands significant resources. Although DEMs (Digital Elevation Models) are mostly publicly available by government agencies, their coarse resolution limits their localization accuracy (Tomešek et al., 2022).

SLAM datasets incorporating both aerial and ground platforms (Dubois et al., 2020; Zhu et al., 2023; Chaney et al., 2023; Zhao et al., 2024; Zhou et al., 2024), as well as multiple ground-based platforms (Feng et al., 2024; Tian et al., 2023), have been published. Nevertheless, these datasets typically cover only limited areas. CS-CAMPUS3D (Guan et al., 2023) is a dataset for point cloud place recognition task with self-collected ground LiDAR scans and aerial LiDAR scans from the state government. However, this task can only yield coarse localization results. D-GLSNet (Li et al., 2023b) provides a dataset of satellite images aligned with point clouds from KITTI (Geiger et al., 2012) for 2D-3D matching. Nonetheless, the matching results are limited to 3-DoF poses, providing only horizontal positions and a heading angle.

2.2. Cross-modal localization and dataset

Many Image-to-Point Cloud (I2P) algorithms have been developed to solve the cross-modal localization problem. Deep learning techniques have been used to build correspondences between image key points and point clouds. P2-Net (Wang et al., 2021) matches pixel and point directly by jointly learned feature description. CoFiI2P (Kang et al., 2024) proposed a coarse-to-fine pipeline for progressive alignment. DeepI2P (Li and Lee, 2021) converts the registration problem to a classification task to avoid building correspondences between two modalities. Extrinsic calibration between LiDARs and cameras is a task for accurate registration results. Some solutions are constrained by artificial targets like Apriltags (Xie et al., 2018), and checkerboards (Huang et al., 2024). For targetless calibration, geometric features like lines (Zhang et al., 2021), edges (Li et al., 2024c), planes (Chai et al., 2018) and vanishing points (Bai et al., 2020) have been exploited. Extrinsic can also be solved after ego-motion of each sensor has been estimated (Park et al., 2020). Semantic features are considered for both point clouds and images (Luo et al., 2024).

Visual SLAM in prior point cloud maps is another task in cross-modal localization. Feature-based methods establish constraints between 2D image and 3D maps features. Line features are extracted from both images and point clouds and subsequently matched in a VIO system (Zheng et al., 2024). HyperMap (Chang et al., 2021) leverages 3D sparse convolution to extract and compress features for the point cloud map. Registration-based methods typically align image point clouds with prior LiDAR maps (Zuo et al., 2019). Depth images from point cloud maps and stereo cameras can be aligned for localization (Kim et al., 2018). Semantic information such as lane lines and road markings can also be applied for visual localization (Qin et al., 2021).

In general, current cross-modal localization solutions predominantly operate on single-platform datasets, such as those captured from cars (Geiger et al., 2013; Caesar et al., 2020), backpacks (Wang et al., 2020), handheld devices (Helmberger et al., 2022; Ramezani et al., 2020), helmets (Li et al., 2023a), UAVs (Nguyen et al., 2022; Thalagala et al., 2024; Li et al., 2024a), and UGVs (Yin et al., 2021; Feng et al., 2024). The applicability to datasets from aerial and ground platforms—such as GRACO (Zhu et al., 2023), M3ED (Chaney et al., 2023), SubT-MRS (Zhao et al., 2024) and CoPeD (Zhou et al., 2024)—remains constrained.

2.3. Ground truth trajectory Generation

Ground truth trajectories serve as a benchmark for SLAM evaluation (Li et al., 2023a) and deep learning training (Kang et al., 2024). Methods that directly refine and optimize maps, such as photogrammetry (Majdik et al., 2017) and LiDAR scan matching (Carlevaris-Bianco et al., 2016), derive ground truth trajectories by enhancing map consistency. However, they rely on revisited areas, the availability of which is environment-dependent, making the ground truth generation variable across different scenarios. Beyond leveraging map features, ground truth trajectories can also

Table 1

Number of image–ALS point cloud pairs for each sequence across the three datasets.

Dataset	Sequence	Pairs
California	3350	4,960
	0248	3,923
	0411	1,384
	4706	1,611
	5828	6,943
	1211	7,780
Hong Kong	1451	7,082
	Deep	6,579
	Harsh	6,870
	Medium	3,137
Wuhan	Loop 1	8,526
	Loop 2	5,206
	Loop 3	5,663

be acquired using external reference systems, including RTK (Thalagala et al., 2024), RTK/INS (Hsu et al., 2023), motion capture system (Schubert et al., 2018), total station (Yin et al., 2021; Nguyen et al., 2022), control point (Schaer and Vallet, 2016), TLS point clouds (Zhao et al., 2024; Zhang et al., 2022) and fiducial marker (Zhou et al., 2024). Nevertheless, these methods are laborious for large-scale areas and restricted by visibility conditions. In addition, ground truth trajectories may become less reliable due to GNSS multipath effects (Hsu et al., 2023; Wen et al., 2020), failures in LiDAR scan matching (Ramezani et al., 2020), and the diminishing effectiveness of ground surveys for large-scale trajectory refinement (Mao et al., 2015) in real-world scenarios. Our method indirectly generates ground-truth poses by registering mobile laser scanning (MLS) submaps to pre-georeferenced airborne laser scanning (ALS) point clouds and optimizing a pose graph. Leveraging the global coverage of ALS, it avoids reliance on revisited areas and significantly reduces labor.

3. Dataset description

Our dataset integrates ground-level imagery and aerial laser scanning (ALS) data collected in three major urban cities—Hong Kong, San Francisco, and Wuhan—using various mobile mapping systems. This section outlines the geographic coverage, sensing modalities, and platform configurations for each region.

3.1. Study area

As shown in Figure 1, the Hong Kong, San Francisco, and Wuhan datasets are selected for their unique advantages. All datasets cover both commercial cores and residential neighborhoods. For instance, the San Francisco dataset includes data collected from Market Street, a major transit artery, and Russian Hill, which reflects typical residential areas. Similarly, the Hong Kong dataset covers Tsim Sha

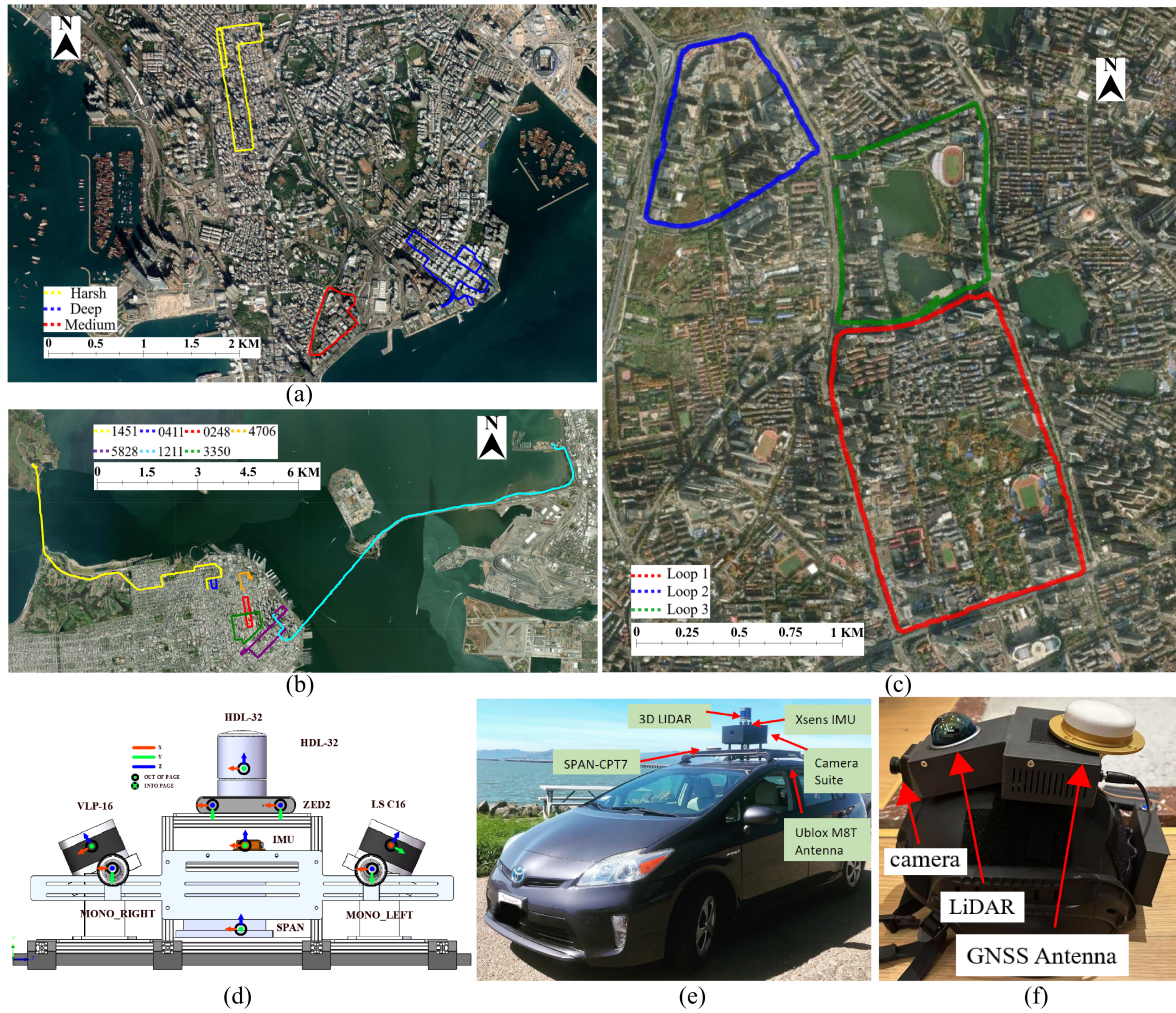


Fig. 2. Dataset coverage and collection. (a), (b) and (c) illustrate trajectories of the Hong Kong, California and Wuhan datasets, while (d), (e) and (f) are the corresponding data acquisition platforms, with (d) and (e) provided by authors of UrbanNav (Hsu et al., 2023) and UrbanLoco (Wen et al., 2020), respectively.

Tsui and Nathan Road, two of Hong Kong’s busiest commercial districts, as well as Whampoa, a large-scale residential zone. The Wuhan dataset focuses on the Hankou area, which contains dense urban blocks and bustling commercial streets. In addition, a variety of terrains are included, such as flat areas (e.g., Tsim Sha Tsui), hilly regions (e.g., Russian Hill), and elevated infrastructure (e.g., the Golden Gate Bridge). Lastly, these three cities are representative global megacities for their high urban densities, making the datasets valuable for cross-view and cross-modal localization tasks. The trajectories and data acquisition platforms are illustrated in Figure 2.

3.2. Ground platform

The ground datasets leveraged in this paper originate from UrbanNav (Hsu et al., 2023) and UrbanLoco (Wen et al., 2020), both of which offer multimodal data (i.g. LiDAR, camera, IMU, GNSS and INS/GNSS) operating in highly-urbanized environments.

UrbanNav (Hsu et al., 2023): The Hong Kong subset of the UrbanNav dataset has been selected. To construct our dataset, only the horizontal LiDAR (HDL-32E Velodyne) and the ZED2 camera are utilized. The reference trajectory is derived from SPAN-CPT. The tunnel dataset is excluded due to LiDAR degeneration and the lack of aerial data coverage. The combined trajectory length of the remaining three datasets—Medium, Deep, and Harsh—exceeds 13 kilometers.

UrbanLoco (Wen et al., 2020): The San Francisco subset of the UrbanLoco dataset has been selected, featuring a RoboSense 32-line LiDAR and six 360-degree view cameras. The reference trajectory is obtained from SPAN-CPT. Collectively, the seven datasets cover a total trajectory length of over 35 kilometers.

WHU-Helmet (Li et al., 2023a): We collected three trajectory loops in Wuhan using WHU-Helmet, a helmet-based mobile mapping system equipped with a Mid360 LiDAR, a camera, and a GNSS antenna. The data were mainly acquired

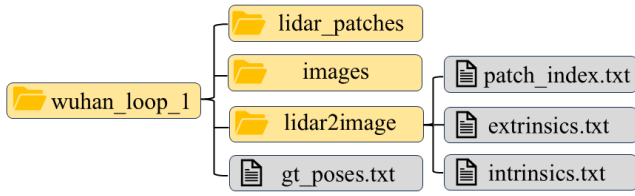


Fig. 3. File structure of the dataset (taking Wuhan Loop 1 as an example).

along sidewalks in dense urban environments, with a total trajectory length exceeding 11 km.

3.3. Aerial platform

The aerial data incorporated into our dataset consists of publicly available ALS point clouds obtained from government agencies in Hong Kong (CEDD, Hong Kong, 2020) and San Francisco (USGS, U.S.A., 2023). These 3D point clouds are acquired using airborne LiDAR sensors, making them particularly valuable for 6-DoF localization tasks compared to 3-DoF localization methods that rely on 2D maps (e.g., satellite imagery, OpenStreetMap).

Hong Kong ALS data (CEDD, Hong Kong, 2020): Acquired in 2020, the Hong Kong ALS point clouds (CEDD, Hong Kong, 2020) have an average point spacing of 0.25 meters. Accuracy assessments based on checkpoints indicate a vertical precision of 0.1 meters on flat open terrain, while the horizontal accuracy is measured at 0.3 meters.

San Francisco ALS data (USGS, U.S.A., 2023): San Francisco B23 LiDAR (USGS, U.S.A., 2023) was collected in 2023, with an average point spacing of 0.15 meters. Based on 30 checkpoints in non-vegetated areas, the vertical accuracy is 0.196 meters. Taking into account factors such as flying altitude, IMU error, and GNSS positional error, the horizontal accuracy is calculated to be 0.12 meters.

Wuhan ALS data: Collected in 2024, the ALS point clouds of Wuhan cover densely urbanized areas of Hankou, with an average point spacing of 0.15 m and an average horizontal accuracy of 20 cm.

3.4. Data overview

The file structure of the dataset is illustrated in Figure 3. Each sequence contains four components: a folder of aerial LiDAR (ALS) patches, a folder of ground images, a text file containing ground-truth poses, and a folder for projecting ALS point clouds onto the ground images. Table 1 demonstrates the distribution of image–ALS point cloud pairs across sequences.

ALS patches: All aerial LiDAR point clouds are downsampled to a resolution of 0.5 meters. To improve processing efficiency, the downsampled point clouds are further divided into patches of 100 m² each.

Images: To reduce computational load, images from Wuhan and California are downsampled by 50% and 25%, respectively. Images are sampled along the trajectory at intervals of 0.5 meters, and each image corresponds to a specific LiDAR patch.

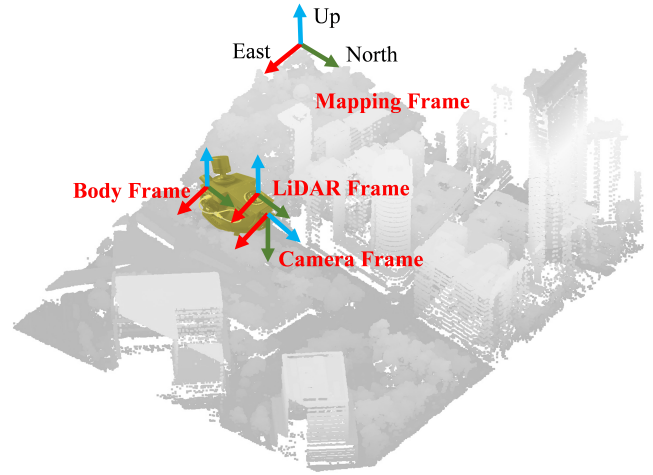


Fig. 4. Definition of coordinate frames.

ALS to image projection: To enable the projection of ALS patches onto ground images, the dataset provides the extrinsic calibration between the ground LiDAR and camera, as well as the camera intrinsics. In addition, the file `patch_index.txt` records the pairing between each image (*.jpg), its corresponding ALS patch (*.las), and the center coordinate of that patch.

Ground-truth trajectory: Each line in the pose file (.txt format) contains 16 values representing a 4×4 transformation matrix. These poses describe the ground LiDAR positions in the mapping frame (ENU frame). To project a 3D ALS point onto the image plane, the following equation is used:

$$\mathbf{p}_{\text{img}} = \mathbf{P}\mathbf{T}_{\text{ext}}\mathbf{T}^{-1}\mathbf{p}_{\text{als}}, \quad (1)$$

where \mathbf{p}_{als} is a homogeneous ALS point, \mathbf{T} is the ground LiDAR pose, \mathbf{T}_{ext} is the extrinsic matrix from ground LiDAR to camera, and \mathbf{P} is the camera intrinsic matrix.

4. Ground truth generation

To obtain accurate 6-DoF ground-truth poses for images, we adopt an indirect strategy: we first align Mobile Laser Scanning (MLS) data from the vehicle platform with ALS point clouds. Since the MLS and camera are rigidly mounted on the same platform, the resulting refined MLS trajectory serves as a proxy to provide accurate image poses by applying calibration parameters. To this end, system states are initialized by aggregating all LiDAR frames. Feature correspondences are then extracted—ground segmentation is applied to MLS data, while roof structures are extracted from ALS point clouds to complete building facades. These multi-source constraints are integrated into a factor graph, through which the optimized MLS trajectory, and hence the image ground-truth poses, are obtained. Figure 4 illustrates the four coordinate frames involved in the ground-truth optimization pipeline, including the mapping frame, LiDAR frame, camera frame, and IMU (body) frame.

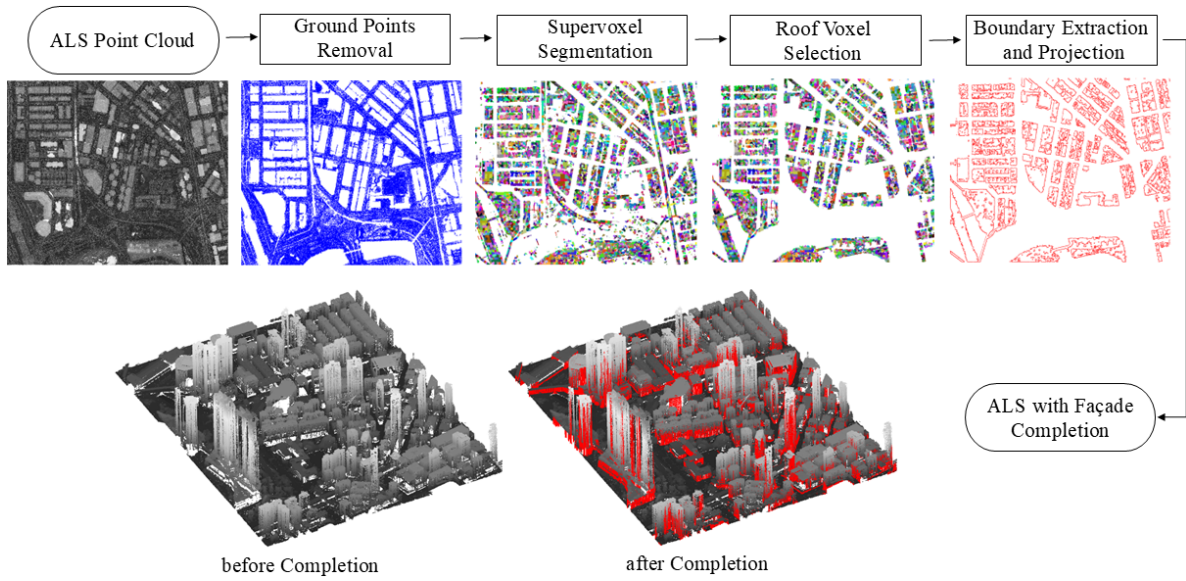


Fig. 5. The flowchart of ALS feature extraction. Gray points represent the original ALS point clouds (rendered in grayscale based on elevation values) while red points indicate the projected façade points.

4.1. Formulation

Let \mathbf{X}_k denote the state of the k -th point cloud frame. The full state vector is defined as follows:

$$\mathcal{X} = [\mathbf{X}_0, \mathbf{X}_1, \dots, \mathbf{X}_n], \quad (2)$$

$$\mathbf{X}_k = [\mathbf{t}_k, \mathbf{v}_k, \omega_k, \mathbf{b}_k^a, \mathbf{b}_k^g], \quad k \in [0, n], \quad (3)$$

where \mathbf{t}_k , \mathbf{v}_k , and ω_k represent the position, velocity, and Lie algebra of rotation matrix $\mathbf{R}_k \in \text{SO}(3)$, respectively. \mathbf{b}_k^a and \mathbf{b}_k^g denote the accelerometer and gyroscope biases. n is the total number of states.

4.2. Correspondences extraction between MLS and ALS

To select salient features for MLS and ALS matching, the MLS point clouds are classified into ground and non-ground points. For each MLS scan, points having the highest planarity (Weinmann et al., 2015) and the lowest verticality (Demantké et al., 2012) are identified as initial ground plane seeds, which are then used to fit the ground plane using the RANSAC (FISCHLER AND, 1981) algorithm.

Ground points in ALS, which help to correct vertical position errors as well as roll and pitch angles in the MLS trajectory, have already been classified. To further eliminate errors in the horizontal position and heading angle of the MLS trajectory, we leverage ALS building point clouds as reliable features. To extract building point clouds, non-ground points are first segmented into supervoxels (Lin et al., 2018), which are then merged with neighboring supervoxels based on voxel normals and centroids. Supervoxels with planarity (Weinmann et al., 2015) greater than 0.5 and verticality (Demantké et al., 2012) less than 0.3 are classified as building roof points. To address gaps in the ALS point clouds on building facades, roof boundaries are extracted using a

convex hull and projected onto the ground to complete the facade points. Figure 5 demonstrates the workflow of ALS feature extraction, where the point clouds are enhanced with facade points.

4.3. Pose graph optimization

To obtain high-precision ground-truth trajectories, we formulate a tightly coupled multi-sensor pose graph optimization framework. Each node in the graph represents the complete state of a LiDAR frame, including the platform's pose, velocity, and inertial measurement unit (IMU) biases. The full state vector is defined as:

$$\mathcal{X} = \{\mathbf{X}_0, \mathbf{X}_1, \dots, \mathbf{X}_N\}, \quad \mathbf{X}_i = (\mathbf{R}_i, \mathbf{t}_i, \mathbf{v}_i, \mathbf{b}_i^a, \mathbf{b}_i^g). \quad (4)$$

The cost function is defined as the weighted sum of residuals from five types of factors:

$$\min_{\mathcal{X}} \sum_{i,j} \|\mathbf{r}_{\text{loop}}^{i,j}\|_{\Lambda_{\text{loop}}^{i,j}}^2 + \sum_i \|\mathbf{r}_{\text{aerial}}^i\|_{\Lambda_{\text{aerial}}^i}^2 + \sum_i \|\mathbf{r}_{\text{imu}}^{i,i+1}\|_{\Lambda_{\text{imu}}^{i,i+1}}^2 + \sum_i \|\mathbf{r}_{\text{gnss}}^i\|_{\Lambda_{\text{gnss}}^i}^2 \quad (5)$$

$$+ \sum_i \|\mathbf{r}_{\text{odometer}}^{i,i+1}\|_{\Lambda_{\text{odometer}}^{i,i+1}}^2, \quad (6)$$

where each Λ denotes the information matrix associated with the corresponding residual term.

Loop closure constraints are introduced by detecting revisited submap pairs via an intersection-over-union (IoU) threshold. Local 3D features, including the Intrinsic Shape Signatures (ISS) keypoints and Binary Shape Context (BSC) descriptors, are used to estimate the relative transformation $(\hat{\mathbf{R}}_{i,j}, \hat{\mathbf{t}}_{i,j})$. The resulting residual is:

$$\mathbf{r}_{\text{loop}}^{i,j} = \begin{bmatrix} \log \left(\hat{\mathbf{R}}_{i,j}^{-1} (\mathbf{R}_i^{-1} \mathbf{R}_j) \right) \\ \mathbf{R}_i^{-1} (\mathbf{t}_j - \mathbf{t}_i) - \hat{\mathbf{t}}_{i,j} \end{bmatrix}. \quad (7)$$

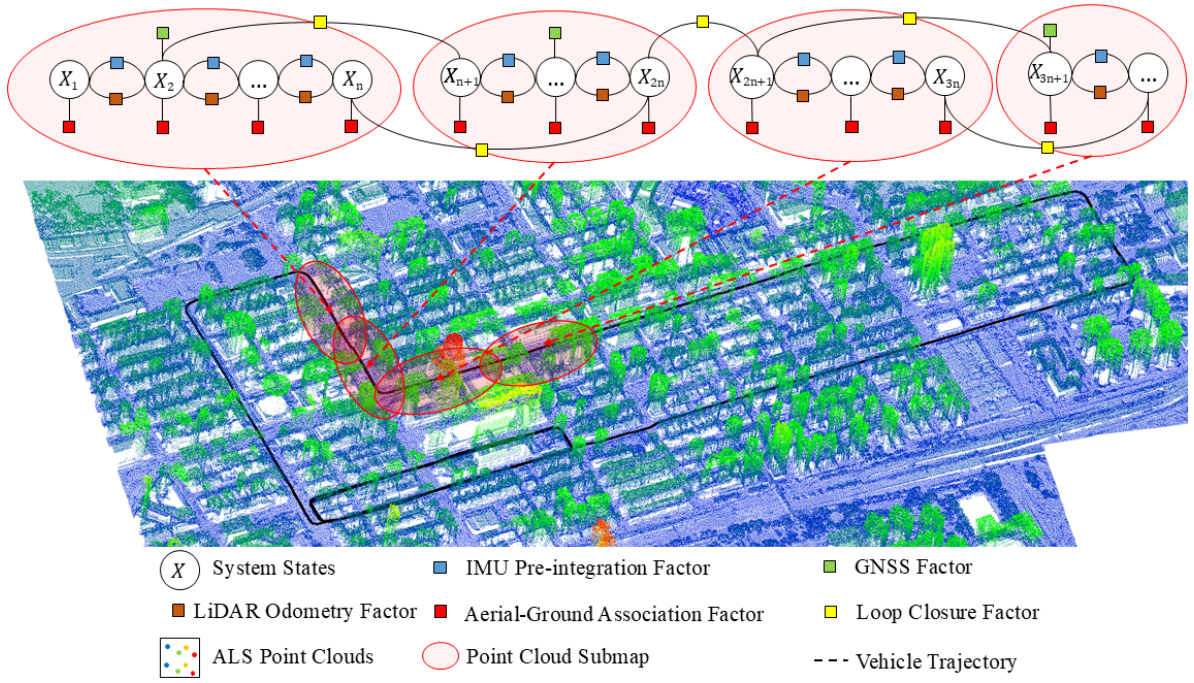


Fig. 6. Pose graph formulation for ground-truth generation.

Aerial-ground constraints are derived by registering MLS submaps to ALS point clouds using Iterative Closest Point (ICP). The alignment residual is:

$$\mathbf{r}_{\text{aerial}}^i = \begin{bmatrix} \log \left(\hat{\mathbf{R}}_{\text{aerial}}^{-1} \mathbf{R}_i \right) \\ \mathbf{t}_i - \hat{\mathbf{t}}_{\text{aerial}} \end{bmatrix}. \quad (8)$$

Odometry constraints model the relative motion between consecutive LiDAR frames:

$$\mathbf{r}_{\text{odom}}^{i,i+1} = \begin{bmatrix} \log \left(\hat{\mathbf{R}}_{i,i+1}^{-1} (\mathbf{R}_i^{-1} \mathbf{R}_{i+1}) \right) \\ \mathbf{R}_i^{-1} (\mathbf{t}_{i+1} - \mathbf{t}_i) - \hat{\mathbf{t}}_{i,i+1} \end{bmatrix}. \quad (9)$$

IMU pre-integration factors are introduced to capture inertial constraints between LiDAR scans. The residual is defined as:

$$\mathbf{r}_{\text{imu}}^{i,i+1} = \begin{bmatrix} \delta \alpha_{i+1}^i \\ \delta \beta_{i+1}^i \\ \delta \gamma_{i+1}^i \\ \delta \mathbf{b}^a \\ \delta \mathbf{b}^g \end{bmatrix}, \quad (10)$$

$$= \begin{bmatrix} \mathbf{R}_i^{-1} \left(\mathbf{t}_{i+1} - \mathbf{t}_i - \mathbf{v}_i \Delta t + \frac{1}{2} \mathbf{g} \Delta t^2 \right) - \hat{\alpha}_{i+1}^i \\ \mathbf{R}_i^{-1} (\mathbf{v}_{i+1} - \mathbf{v}_i + \mathbf{g} \Delta t) - \hat{\beta}_{i+1}^i \\ \log \left((\hat{\gamma}_{i+1}^i)^{-1} \mathbf{R}_i^{-1} \mathbf{R}_{i+1} \right) \\ \mathbf{b}_{i+1}^a - \mathbf{b}_i^a \\ \mathbf{b}_{i+1}^g - \mathbf{b}_i^g \end{bmatrix}. \quad (11)$$

Here, $\hat{\alpha}_{i+1}^i$, $\hat{\beta}_{i+1}^i$, and $\hat{\gamma}_{i+1}^i$ are the pre-integrated position, velocity, and rotation increments, respectively. \mathbf{g} denotes the gravity vector, and Δt is the integration time interval.

GNSS constraints incorporate RTK-based absolute position measurements with lever-arm compensation:

$$\mathbf{r}_{\text{gnss}}^i = \mathbf{t}_i + \mathbf{R}_i \cdot \mathbf{t}_{\text{ant}} - \hat{\mathbf{t}}_i^{\text{GNSS}}, \quad (12)$$

where \mathbf{t}_{ant} represents the lever arm from the platform center to the GNSS antenna.

The overall nonlinear least squares problem is solved via the Levenberg–Marquardt algorithm (Moré, 2006), with computational efficiency enhanced by sparse matrix factorization using SuiteSparse (Davis, 2018). Figure 6 illustrates the pose graph optimization framework. The MLS point clouds are segmented into multiple submaps, each constrained by four types of factors: the aerial-ground association factor, the GNSS factor, the IMU pre-integration factor, and the LiDAR odometry factor. Loop closure factors are introduced to establish connections between submaps with revisited areas.

5. Ground truth evaluation

To assess the accuracy and effectiveness of the generated ground-truth trajectories, both qualitative and quantitative evaluations are conducted. Three representative scenes are selected for evaluation: the medium dataset in Urban-Nav (Hsu et al., 2023), the Bay Bridge dataset from Urban-LoCo (Wen et al., 2020), and the Loop 1 dataset in Wuhan.

5.1. Qualitative evaluation

To qualitatively evaluate the optimized trajectories, we project the ALS point clouds onto the vehicle cameras. This approach offers an intuitive means of assessing the ground-truth trajectory. Representative scenarios of the



Fig. 7. Projection of ALS point clouds to images. (a), (b) and (c) are from Wuhan, Hong Kong and California datasets, respectively. Point clouds are colorized by depth, with colors ranging from blue (near) to red (far), through green and yellow.

Table 2

Check point errors with generated ground truth trajectories.

Sequence	Check point error (m)		
	Avg.	Min.	Max.
California Bay Bridge	0.16	0.11	0.23
Hong Kong Medium	0.11	0.07	0.15
Wuhan Loop 1	0.09	0.03	0.12

three datasets are displayed in Figure 7. Visualizations show a well-aligned projection, where both geometric structures and depth cues are clearly consistent. Besides, the improved MLS point cloud quality demonstrates the effectiveness of the trajectory generation. As shown in Figures 8, 9, and 10, the MLS point clouds are better aligned with the ALS point clouds, where blue and red points represent the point clouds before and after optimization, respectively.

5.2. Quantitative evaluation

As shown in Figures 8, 9, and 10, several checkpoints were manually selected and aligned between the MLS and ALS point clouds to evaluate the accuracy of the trajectory. These significant feature points are primarily located at the corners of pedestrian overpasses and buildings. According to 2, in the dense urban datasets of Hong Kong Medium and Wuhan Loop 1, the average checkpoint errors are 11 cm and 9 cm, respectively. In contrast, the California Bay Bridge dataset yields a higher average error of 0.16 m due to its long span. Details of check point errors are presented in Table 2.

6. Benchmarks on SOTA algorithms

6.1. I2P global localization

Three learning-based baseline methods were selected to evaluate the performance of image-to-point cloud (I2P) global localization on our dataset, including:

AE-Spherical (Zhao et al., 2023), is the first to achieve end-to-end cross-modality visual localization. It uses point clouds generated by multi-beam vehicle-borne LiDAR point

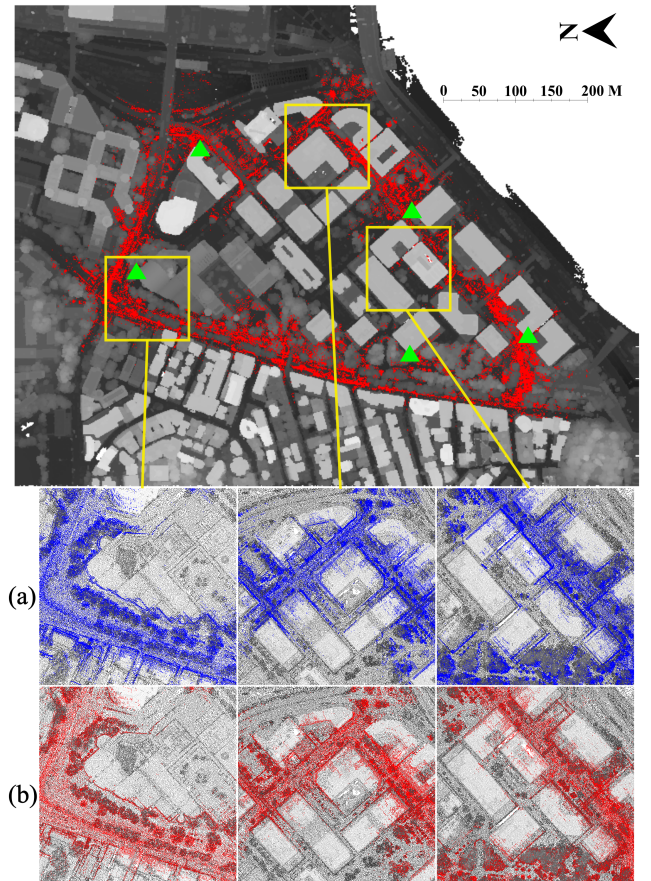


Fig. 8. Point cloud refinement of the Hong Kong Medium dataset. (a) and (b) illustrate the MLS point clouds before and after optimization. ALS points are rendered in grayscale to represent relative elevation, while green triangles indicate the check points.

clouds as the map representation and panoramic images as input, aligning multi-modality data through a feature representation learning architecture. In the image branch, AE-Spherical employs a spherical CNN-based backbone

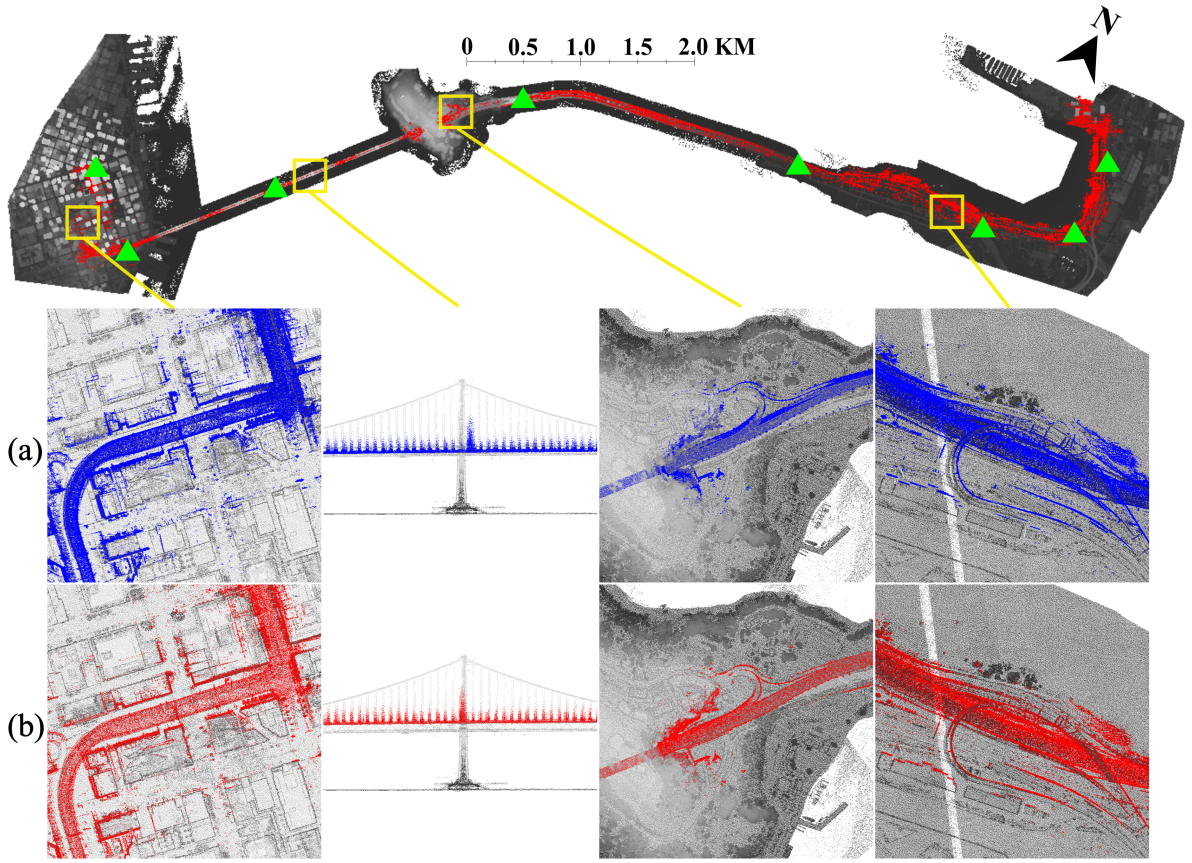


Fig. 9. Point cloud refinement of California Bay Bridge dataset. (a) and (b) illustrate the MLS point clouds before and after optimization. ALS points are rendered in gray to represent relative height, while green triangles indicate the check points.

for feature extraction, followed by NetVLAD (Arandjelović et al., 2018) aggregation to obtain global descriptors. In the point cloud branch, it directly employs PointNetVLAD (Uy and Lee, 2018) to generate global features. Furthermore, the channel attention (Hu et al., 2018) is incorporated into both branches to enhance feature representation and improve cross-modality alignment performance. We modified the feature backbone by replacing the spherical CNN with ResNet and maintaining other modules unchanged. We retrained their model¹ on our datasets.

LIPLoc (Shubodh et al., 2024), which first projects the point cloud into a depth map and then aligns the RGB image and the depth map in a high-dimensional feature space using a contrastive learning paradigm, thereby achieving cross-modal coarse visual localization. Specifically, the point cloud frames are converted into range images based on the scan pattern of the LiDAR sensor. The input images are resized to 224×224 , and then a visual transformer-based feature encoder along with a linear projection layer is employed to generate global features for both the images and the range images. We retrained their model² using their default parameters on our datasets.

SaliencyI2PLoc (Li et al., 2025b), a novel contrastive learning-based architecture that integrates saliency maps

into the feature aggregation process and preserves feature relationship consistency across multiple manifold spaces. To reduce the need for extensive data mining in the preprocessing stage, a contrastive learning framework is employed to effectively establish cross-modality feature mappings. A context saliency-guided local feature aggregation module is proposed to exploit stationary scene information, thereby generating more representative global features. Additionally, to further improve cross-modal feature alignment during contrastive learning, the model incorporates the consistency of relative sample relationships across different manifold spaces. We retrained their model³ on our datasets.

Following the SaliencyI2PLoc (Li et al., 2025b), the recall value is utilized to evaluate the I2P global localization quantitative performance. For the California dataset, we select the 0411 and 4701 sequence to assess the performance, while the part of Deep sequence of Hong Kong dataset and Loop-1 sequence of Wuhan dataset are chosen to be the evaluation dataset, respectively. We establish almost 14k and 15k image-point cloud pairs from Hong Kong and Wuhan dataset to train the model. The evaluation dataset is not contained in the training dataset. The AE-Spherical baseline requires the construction of positive and negative sample pairs, we collected the query image every 3 m and set the

¹<https://github.com/Zhaozhpe/AE-CrossModal>

²<https://github.com/Shubodh/lidar-image-pretrain-VPR>

³<https://github.com/whu-lyh/SaliencyI2PLoc>

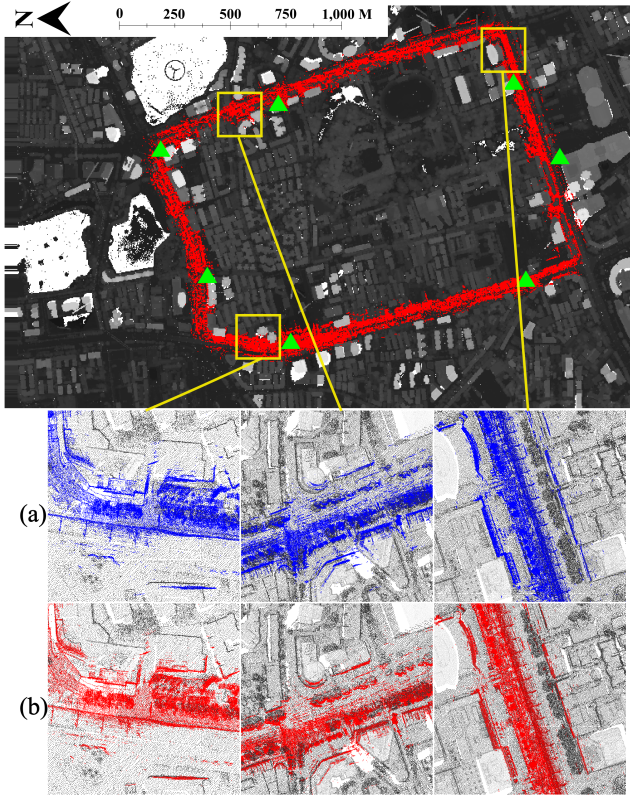


Fig. 10. Point cloud refinement of the Wuhan Loop 1 dataset. (a) and (b) illustrate the MLS point clouds before and after optimization. ALS points are rendered in grayscale to represent relative elevation, while green triangles indicate the check points.

Table 3
The dataset details.

	CA			HK			HK		
	Query	Database	Total	Query	Database	Total	Query	Database	Total
Train	-	-	-	-	-	14100	-	-	15551
Evaluation	-	-	-	206	2280	2486	664	3180	3844

radius distance to be 20 m and 40 m to classify the positives and negatives. The detail of the dataset splitting is listed in Table 3.

The quantitative results on the California, Hong Kong, and Wuhan datasets are presented in Table 4 and Table 5. LIPLoc (Shubodh et al., 2024) employs projected images as proxies to bridge the modality gap between images and point clouds, thereby achieving the best performance across all evaluated datasets. In contrast, both SaliencyI2PLoc (Li et al., 2025b) and AE-Spherical (Zhao et al., 2023) directly operate on raw point clouds. Due to differences between airborne and vehicle-mounted point clouds—such as variations in point density, noise characteristics, and spatial distribution—these two methods demonstrate limited effectiveness in cross-modality localization. Although SaliencyI2PLoc slightly outperforms AE-Spherical, particularly on the Hong Kong and Wuhan sequences, LIPLoc consistently achieves

Table 4

I2P global localization recall values on the California dataset.

Method	0411 sequence			4706 sequence		
	R1(%) ↑	R5(%) ↑	R20(%) ↑	R1(%) ↑	R5(%) ↑	R20(%) ↑
AE-Spherical (Zhao et al., 2023)	8.76	13.87	16.79	24.36	30.77	35.90
LIPLoc (Shubodh et al., 2024)	13.14	30.66	47.45	16.67	34.62	53.85
SaliencyI2PLoc (Li et al., 2025b)	8.03	11.68	16.06	19.23	23.08	24.36

Table 5

I2P global localization recall values on the Hong Kong dataset and Wuhan dataset.

Method	Deep sequence			Loop-1 sequence		
	R1(%) ↑	R5(%) ↑	R20(%) ↑	R1(%) ↑	R5(%) ↑	R20(%) ↑
AE-Spherical (Zhao et al., 2023)	10.68	14.56	17.96	3.61	5.87	8.43
LIPLoc (Shubodh et al., 2024)	19.90	35.92	60.19	16.50	35.44	54.85
SaliencyI2PLoc (Li et al., 2025b)	20.87	22.82	24.27	6.48	7.68	10.09

superior results across all metrics. Given the broader coverage and higher acquisition efficiency of airborne LiDAR compared to vehicle-mounted systems, vision-based localization using airborne point clouds offers greater potential for real-world applications. Nonetheless, the current performance of both SaliencyI2PLoc and AE-Spherical remains far from practical usability, highlighting substantial room for future improvement.

6.2. I2P fine localization

To address fine-grained localization between images and point clouds, we evaluated three representative learning-based I2P registration methods: DeepI2P (Li and Lee, 2021), CorrI2P (Ren et al., 2022), and CoFilI2P (Kang et al., 2024) with their official implementations, adapted and retrained on our dataset. A brief overview of each method is provided below.

DeepI2P (Li and Lee, 2021): reformulates image-to-point cloud pose estimation as a two-stage classification and optimization problem. Instead of learning explicit descriptors for point cloud and image, it uses a two-branch classification network with attention-based image–point cloud fusion to predict whether each 3D point lies inside the camera frustum, thus reducing reliance on handcrafted key-points and feature matching. A inverse camera projection solver then recovers the relative camera-to-LiDAR transformation from the classification results. This design bypasses direct point-to-pixel correspondence estimation, minimizes storage, and remains robust under challenging viewpoint and modality gaps. We retrained the official model⁴ on our dataset.

CorrI2P (Ren et al., 2022): treats the image-to-point cloud registration as a dense correspondence estimation task. It employs a dual-branch architecture for modality-specific feature extraction and a multi-scale fusion mechanism to progressively integrate contextual cues. A confidence-guided correspondence regression module improves match reliability, while a transformation estimation layer jointly

⁴<https://github.com/lijx10/DeepI2P>

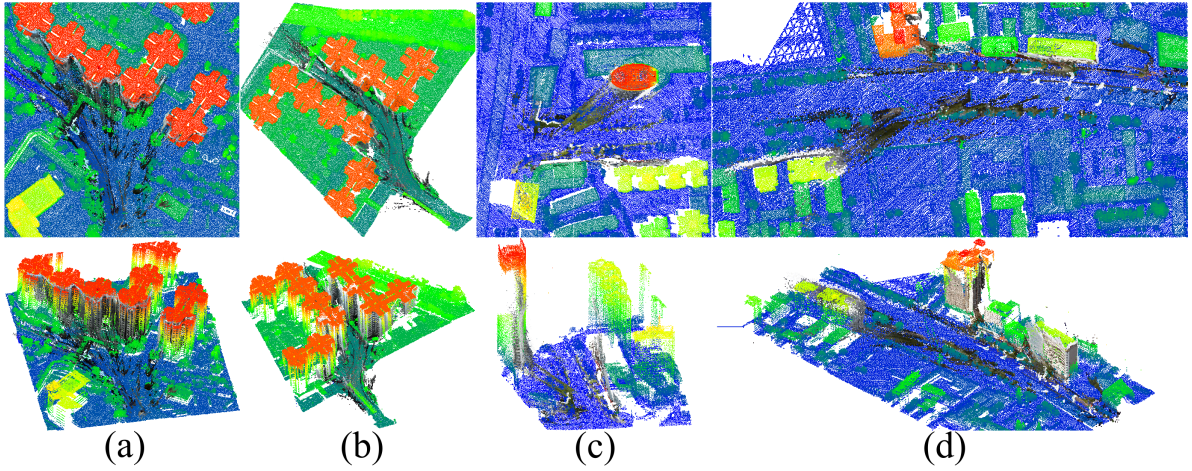


Fig. 11. I2P fine localization results. Dark points are from dense matching of images, and ALS point clouds are colorized by height.

refines rotation and translation parameters. This design enhances robustness under large viewpoint changes and modality gaps. We retrained the official model⁵ on our dataset.

CoFiI2P (Kang et al., 2024): adopts a coarse-to-fine strategy, combining global pose initialization with local refinement. The coarse stage estimates an approximate transformation from global context features, while the fine stage iteratively refines the pose using local geometry and semantic cues. A confidence-guided correspondence filtering mechanism suppresses noisy matches, balancing efficiency and accuracy in complex scenes. We retrained the official model⁶ on our dataset.

Despite careful adaptation, none of these methods succeeded in producing reliable correspondences or accurate relative poses in our data. We attribute this primarily to the lack of structured objects in our scenes (e.g., poles, traffic signs, other salient landmarks) that are crucial for cross-modal matching. In contrast to image-LiDAR pairs acquired simultaneously by the same platform, our aerial-based point clouds and vehicle-based images suffer from substantial viewpoint and acquisition-time discrepancies, further exacerbating the registration challenge. Specifically, DeepI2P, which depends on dense pixel-to-point similarity learning, is highly sensitive to the absence of distinctive geometric structures, making feature associations in sparse, texture-less regions ambiguous. CorrI2P, which relies on local correspondence matching guided by global priors, fails when repetitive or weak visual cues dominate, leading to unstable matches. CoFiI2P, which depends on accurate coarse alignment, accumulates large errors in its initial stage under severe viewpoint discrepancies, leaving the fine stage ineffective.

After the failure of learning-based approaches, we perform Structure-from-Motion (SfM) on images sampled along the trajectory at intervals of 100 meters and recover the scale using VINS-Mono. Subsequently, we conduct ICP

Table 6

I2P fine localization accuracy on different regions.

Region	RRE(°)	RTE(m)
Hong Kong	4.06 ± 3.29	2.87 ± 2.08
Wuhan	7.80 ± 2.21	2.64 ± 1.25
California	14.54 ± 11.82	4.59 ± 4.14

registration between the dense matching image point clouds and the ALS point clouds. Figure 11 demonstrates the I2P fine localization results. The registration accuracy is assessed using Relative Rotation Error (RRE) and Relative Translation Error (RTE). The Euler angle vector \mathbf{r} is derived from the relative rotation matrix $\mathbf{R}_{gt}^{-1}\mathbf{R}_e$, where \mathbf{R}_{gt} and \mathbf{t}_{gt} denote the ground-truth rotation and translation and \mathbf{R}_e and \mathbf{t}_e denote the estimated rotation and translation.

$$\text{RRE} = \sum_{i=1}^3 |\mathbf{r}_i|, \quad \text{RTE} = \|\mathbf{t}_{gt} - \mathbf{t}_e\|_2. \quad (12)$$

The quantitative results for different regions are summarized in Table 6. In Hong Kong dataset, the method achieves the best accuracy, with an RRE of 4.06° and an RTE of 2.87 meters. Wuhan shows slightly higher rotational error (7.80°) but a similar translational error (2.64 meters). California exhibits the largest errors among the three regions, with an RRE of 14.54° and an RTE of 4.59 meters. In particular, the California dataset contains cross-sea bridges and dense urban areas (e.g. Chinatown), where repetitive structures and occlusions further complicate image matching.

7. Challenge issues and future directions

Our experimental results underscore the limitations of current state-of-the-art methods when applied to large-scale,

⁵<https://github.com/rsy6318/CorrI2P>

⁶<https://github.com/WHU-USI3DV/CoFiI2P>

real-world, and cross-platform scenarios. In the following, we highlight key open problems in the field and discuss potential research directions to advance the robustness, scalability, and practicality of cross-modal localization systems.

7.1. Modality discrepancy and cross-domain generalization

As evidenced in Section 6, existing I2P models such as AE-Spherical and SaliencyI2PLoc suffer from degraded performance when applied to cross-modal and cross-view scenarios, especially in the California dataset. This is largely due to the large modality gap between perspective ground-view images and top-down ALS point clouds, compounded by viewpoint and appearance variations.

Many current models still depend heavily on modality-specific features—such as texture patterns in images or height variations in point clouds—which limits their ability to generalize across modalities. Addressing this issue calls for approaches that can extract features robust to both modality and domain changes. Promising directions include: (1) domain-adaptive learning to reduce the domain shift between different modalities and environments; (2) learning shared latent spaces that preserve structural and semantic correspondences; and (3) disentangling geometric information from appearance variations to enhance generalizability across modalities and environments.

7.2. Structural inconsistency and scene complexity

Table 6 shows higher localization errors in the California areas, which are dominated by either open-span infrastructure or extremely dense urban blocks. Both scenarios pose significant challenges for cross-modal alignment: the former provides sparse and repetitive geometry with few stable constraints, while the latter presents highly cluttered scenes with severe occlusions, making both dense matching and ICP registration difficult. In contrast, structured urban areas such as Hong Kong and Wuhan, offer denser and more distinctive geometry, leading to more stable matching. This highlights the sensitivity of both learning-based and registration-based methods to geometric completeness and façade continuity. Future research could explore: (1) incorporating semantic segmentation to identify stable structural elements; (2) applying façade completion techniques to recover missing geometry; and (3) leveraging CAD-aligned priors to introduce precise geometric constraints, thereby improving registration robustness in sparse or ambiguous environments.

7.3. Temporal misalignment and appearance change

Current I2P pipelines face significant challenges when aligning datasets collected across different times. In our case, ALS data acquired by governmental agencies and ground imagery from mobile mapping systems are often collected years apart, leading to temporal discrepancies caused by new construction or demolition, vegetation growth or removal, and seasonal appearance changes. These changes

affect both geometry and visual context, making cross-modal correspondence less reliable in both global retrieval and fine registration stages. Future directions include: (1) developing robust feature extractors that identify stable elements across long time spans; (2) adopting change-aware alignment frameworks such as time-conditioned descriptors; and (3) integrating temporal priors (e.g., historical GIS data) to make cross-modal localization more resilient in real-world applications.

7.4. Computational efficiency and deployment readiness

Although learning-based methods demonstrate potential, most require high-end GPUs and long inference times, limiting their applicability in real-time or embedded systems. For example, SaliencyI2PLoc achieves higher recall in the Hong Kong sequence but is computationally intensive, making it less suitable for real-time deployment. Future work could focus on: (1) applying model compression techniques, such as pruning and knowledge distillation, to reduce computational cost; (2) adopting hardware-aware training strategies; and (3) developing edge inference frameworks, thereby enabling efficient and reliable on-device deployment of aerial-ground localization systems in robotics, AR/VR, and wearable applications.

8. Conclusion

We present a new benchmark for aerial-ground cross-modal localization, integrating mobile mapping imagery with ALS point clouds across three major cities. To support accurate evaluation, we propose an indirect ground-truth generation pipeline based on MLS–ALS alignment and pose graph optimization. Experimental results reveal that existing I2P methods still face significant challenges under large-scale, cross-view, and cross-modal conditions, while ALS-based localization offers promising accuracy and stability. Our benchmark provides a standardized platform for evaluating global and fine-grained localization tasks, aiming to advance research in robust, scalable visual localization under real-world urban scenarios.

CRedit authorship contribution statement

Yandi Yang: Conceptualization of this study, Methodology, Software, Validation, Writing – original draft. **Jianping Li:** Conceptualization of this study, Methodology, Writing review. **Youqi Liao:** Methodology, Writing review. **Yuhao Li:** Methodology, Writing review. **Yizhe Zhang:** Data collection, Writing review. **Zhen Dong:** Methodology, Writing review. **Bisheng Yang:** Conceptualization of this study, Writing review. **Naser El-Sheimy:** Conceptualization of this study, Methodology, Writing review, Project administration, Funding acquisition.

9. Declaration of interests

The authors declare that they have no known competing financial interests or personal relationships that could have appeared to influence the work reported in this paper.

References

- Arandjelović, R., Gronat, P., Torii, A., Pajdla, T., Sivic, J., 2018. Netvlad: Cnn architecture for weakly supervised place recognition. *IEEE Transactions on Pattern Analysis and Machine Intelligence* 40, 1437–1451. doi:10.1109/TPAMI.2017.2711011.
- Aubry, M., Maturana, D., Efros, A.A., Russell, B.C., Sivic, J., 2014. Seeing 3d chairs: exemplar part-based 2d-3d alignment using a large dataset of cad models, in: *Proceedings of the IEEE conference on computer vision and pattern recognition*, pp. 3762–3769.
- Bai, Z., Jiang, G., Xu, A., 2020. Lidar-camera calibration using line correspondences. *Sensors* 20, 6319.
- Caesar, H., Bankiti, V., Lang, A.H., Vora, S., Liong, V.E., Xu, Q., Krishnan, A., Pan, Y., Baldan, G., Beijbom, O., 2020. nuscenes: A multimodal dataset for autonomous driving, in: *Proceedings of the IEEE/CVF conference on computer vision and pattern recognition*, pp. 11621–11631.
- Carlevaris-Bianco, N., Ushani, A.K., Eustice, R.M., 2016. University of michigan north campus long-term vision and lidar dataset. *The International Journal of Robotics Research* 35, 1023–1035.
- CEDD, Hong Kong, 2020. Hong Kong LiDAR Data. <https://sdportal.cedd.gov.hk>.
- Chai, Z., Sun, Y., Xiong, Z., 2018. A novel method for lidar camera calibration by plane fitting, in: *2018 IEEE/ASME International Conference on Advanced Intelligent Mechatronics (AIM)*, IEEE. pp. 286–291.
- Chaney, K., Cladera, F., Wang, Z., Bisulco, A., Hsieh, M.A., Korpela, C., Kumar, V., Taylor, C.J., Daniilidis, K., 2023. M3ed: Multi-robot, multi-sensor, multi-environment event dataset, in: *2023 IEEE/CVF Conference on Computer Vision and Pattern Recognition Workshops (CVPRW)*, pp. 4016–4023. doi:10.1109/CVPRW59228.2023.00419.
- Chang, M.F., Mangelson, J., Kaess, M., Lucey, S., 2021. Hypermap: Compressed 3d map for monocular camera registration, in: *2021 IEEE International Conference on Robotics and Automation (ICRA)*, IEEE. pp. 11739–11745.
- Davis, T.A., 2018. Graph algorithms via suitesparse: Graphblas: triangle counting and k-truss, in: *2018 IEEE High Performance extreme Computing Conference (HPEC)*, IEEE. pp. 1–6.
- Demantké, J., Vallet, B., Paparoditis, N., 2012. Streamed vertical rectangle detection in terrestrial laser scans for facade database production. *ISPRS Annals of the Photogrammetry, Remote Sensing and Spatial Information Sciences* 1, 99–104.
- Dubois, R., Eudes, A., Frémont, V., 2020. Airmuseum: a heterogeneous multi-robot dataset for stereo-visual and inertial simultaneous localization and mapping, in: *2020 IEEE International Conference on Multisensor Fusion and Integration for Intelligent Systems (MFI)*, pp. 166–172. doi:10.1109/MFI49285.2020.9235257.
- El-Sheimy, N., Youssef, A., 2020. Inertial sensors technologies for navigation applications: State of the art and future trends. *Satellite navigation* 1, 2.
- Feng, D., Qi, Y., Zhong, S., Chen, Z., Chen, Q., Chen, H., Wu, J., Ma, J., 2024. S3e: A multi-robot multimodal dataset for collaborative slam. *IEEE Robotics and Automation Letters* , 1–8doi:10.1109/LRA.2024.3490402.
- FISCHLER AND, M., 1981. Random sample consensus: a paradigm for model fitting with applications to image analysis and automated cartography. *Commun. ACM* 24, 381–395.
- Geiger, A., Lenz, P., Stiller, C., Urtasun, R., 2013. Vision meets robotics: The kitti dataset. *The international journal of robotics research* 32, 1231–1237.
- Geiger, A., Lenz, P., Urtasun, R., 2012. Are we ready for autonomous driving? the kitti vision benchmark suite, in: *2012 IEEE conference on computer vision and pattern recognition*, IEEE. pp. 3354–3361.
- Guan, T., Muthuselvam, A., Hoover, M., Wang, X., Liang, J., Sathyamoorthy, A.J., Conover, D., Manocha, D., 2023. Crossloc3d: Aerial-ground cross-source 3d place recognition, in: *Proceedings of the IEEE/CVF International Conference on Computer Vision*, pp. 11335–11344.
- Helmberger, M., Morin, K., Berner, B., Kumar, N., Cioffi, G., Scaramuzza, D., 2022. The hilti slam challenge dataset. *IEEE Robotics and Automation Letters* 7, 7518–7525.
- Hsu, L.T., Huang, F., Ng, H.F., Zhang, G., Zhong, Y., Bai, X., Wen, W., 2023. Hong kong urbannav: An open-source multisensory dataset for benchmarking urban navigation algorithms. *NAVIGATION: Journal of the Institute of Navigation* 70.
- Hu, J., Shen, L., Sun, G., 2018. Squeeze-and-excitation networks, in: *2018 IEEE/CVF Conference on Computer Vision and Pattern Recognition*, pp. 7132–7141. doi:10.1109/CVPR.2018.00745.
- Huang, Z., Zhang, X., Garcia, A., Huang, X., 2024. A novel, efficient and accurate method for lidar camera calibration, in: *2024 IEEE International Conference on Robotics and Automation (ICRA)*, IEEE. pp. 14513–14519.
- Jende, P., Nex, F., Gerke, M., Vosselman, G., 2018. A fully automatic approach to register mobile mapping and airborne imagery to support the correction of platform trajectories in gnss-denied urban areas. *ISPRS journal of photogrammetry and remote sensing* 141, 86–99.
- Jeong, H., Shin, J., Rameau, F., Kum, D., 2024. Multi-modal place recognition via vectorized hd maps and images fusion for autonomous driving. *IEEE Robotics and Automation Letters* .
- Kang, S., Liao, Y., Li, J., Liang, F., Li, Y., Zou, X., Li, F., Chen, X., Dong, Z., Yang, B., 2024. Cofii2p: Coarse-to-fine correspondences-based image to point cloud registration. *IEEE Robotics and Automation Letters* .
- Kim, Y., Jeong, J., Kim, A., 2018. Stereo camera localization in 3d lidar maps, in: *2018 IEEE/RSJ International Conference on Intelligent Robots and Systems (IROS)*, IEEE. pp. 1–9.
- Li, H., Zou, Y., Chen, N., Lin, J., Liu, X., Xu, W., Zheng, C., Li, R., He, D., Kong, F., et al., 2024a. Mars-lvig dataset: A multi-sensor aerial robots slam dataset for lidar-visual-inertial-gnss fusion. *The International Journal of Robotics Research* 43, 1114–1127.
- Li, J., Lee, G.H., 2021. Deepi2p: Image-to-point cloud registration via deep classification, in: *Proceedings of the IEEE/CVF Conference on Computer Vision and Pattern Recognition*, pp. 15960–15969.
- Li, J., Nguyen, T.M., Cao, M., Yuan, S., Hung, T.Y., Xie, L., 2025a. Graph optimality-aware stochastic lidar bundle adjustment with progressive spatial smoothing. *IEEE Transactions on Intelligent Transportation Systems* .
- Li, J., Wu, W., Yang, B., Zou, X., Yang, Y., Zhao, X., Dong, Z., 2023a. Whu-helmet: A helmet-based multisensor slam dataset for the evaluation of real-time 3-d mapping in large-scale gnss-denied environments. *IEEE Transactions on Geoscience and Remote Sensing* 61, 1–16.
- Li, J., Yuan, S., Cao, M., Nguyen, T.M., Cao, K., Xie, L., 2024b. Hcto: Optimality-aware lidar inertial odometry with hybrid continuous time optimization for compact wearable mapping system. *ISPRS Journal of Photogrammetry and Remote Sensing* 211, 228–243.
- Li, L., Ma, Y., Tang, K., Zhao, X., Chen, C., Huang, J., Mei, J., Liu, Y., 2023b. Geo-localization with transformer-based 2d-3d match network. *IEEE Robotics and Automation Letters* 8, 4855–4862.
- Li, X., Duan, Y., Wang, B., Ren, H., You, G., Sheng, Y., Ji, J., Zhang, Y., 2024c. Edgecalib: Multi-frame weighted edge features for automatic targetless lidar-camera calibration. *IEEE Robotics and Automation Letters* .
- Li, Y., Li, J., Dong, Z., Wang, Y., Yang, B., 2025b. Saliency2ploc: Saliency-guided image–point cloud localization using contrastive learning. *Information Fusion* 118, 103015. doi:10.1016/j.inffus.2025.103015.
- Liao, Y., Chen, X., Kang, S., Li, J., Dong, Z., Fan, H., Yang, B., 2024a. Osmloc: Single image-based visual localization in openstreetmap with geometric and semantic guidances. *arXiv preprint arXiv:2411.08665* .
- Liao, Y., Kang, S., Li, J., Liu, Y., Liu, Y., Dong, Z., Yang, B., Chen, X., 2024b. Mobile-seed: Joint semantic segmentation and boundary detection for mobile robots. *IEEE Robotics and Automation Letters* .

- Lin, Y., Wang, C., Zhai, D., Li, W., Li, J., 2018. Toward better boundary preserved supervoxel segmentation for 3d point clouds. *ISPRS journal of photogrammetry and remote sensing* 143, 39–47.
- Liu, H., Cao, C., Ye, H., Cui, H., Gao, W., Wang, X., Shen, S., 2024. Lightweight structured line map based visual localization. *IEEE Robotics and Automation Letters* 9, 5182–5189. doi:10.1109/LRA.2024.3387137.
- Luo, Z., Yan, G., Cai, X., Shi, B., 2024. Zero-training lidar-camera extrinsic calibration method using segment anything model, in: 2024 IEEE International Conference on Robotics and Automation (ICRA), pp. 14472–14478. doi:10.1109/ICRA57147.2024.10610983.
- Majdik, A.L., Till, C., Scaramuzza, D., 2017. The zurich urban micro aerial vehicle dataset. *The International Journal of Robotics Research* 36, 269–273.
- Mao, Q., Zhang, L., Li, Q., Hu, Q., Yu, J., Feng, S., Ochieng, W., Gong, H., 2015. A least squares collocation method for accuracy improvement of mobile lidar systems. *Remote sensing* 7, 7402–7424.
- Merat, R., Cioffi, G., Bauersfeld, L., Scaramuzza, D., 2024. Drift-free visual slam using digital twins. *IEEE Robotics and Automation Letters*.
- Moré, J.J., 2006. The levenberg-marquardt algorithm: implementation and theory, in: Numerical analysis: proceedings of the biennial Conference held at Dundee, June 28–July 1, 1977, Springer. pp. 105–116.
- Nassar, S., El-Sheimy, N., 2006. A combined algorithm of improving ins error modeling and sensor measurements for accurate ins/gps navigation. *GPS solutions* 10, 29–39.
- Nguyen, T.M., Yuan, S., Cao, M., Lyu, Y., Nguyen, T.H., Xie, L., 2022. Ntu viral: A visual-inertial-ranging-lidar dataset, from an aerial vehicle viewpoint. *The International Journal of Robotics Research* 41, 270–280.
- Park, C., Moghadam, P., Kim, S., Sridharan, S., Fookes, C., 2020. Spatiotemporal camera-lidar calibration: A targetless and structureless approach. *IEEE Robotics and Automation Letters* 5, 1556–1563.
- Qin, T., Zheng, Y., Chen, T., Chen, Y., Su, Q., 2021. A light-weight semantic map for visual localization towards autonomous driving, in: 2021 IEEE international conference on robotics and automation (ICRA), IEEE. pp. 11248–11254.
- Ramezani, M., Wang, Y., Camurri, M., Wisth, D., Mattamala, M., Fallon, M., 2020. The newer college dataset: Handheld lidar, inertial and vision with ground truth, in: 2020 IEEE/RSJ International Conference on Intelligent Robots and Systems (IROS), IEEE. pp. 4353–4360.
- Ren, S., Zeng, Y., Hou, J., Chen, X., 2022. Corri2p: Deep image-to-point cloud registration via dense correspondence. *IEEE Transactions on Circuits and Systems for Video Technology* 33, 1198–1208.
- Sarlin, P.E., DeTone, D., Yang, T.Y., Avetisyan, A., Straub, J., Malisiewicz, T., Buló, S.R., Newcombe, R., Kotschieder, P., Balntas, V., 2023a. Orienternet: Visual localization in 2d public maps with neural matching, in: Proceedings of the IEEE/CVF Conference on Computer Vision and Pattern Recognition, pp. 21632–21642.
- Sarlin, P.E., Trulls, E., Pollefeys, M., Hosang, J., Lynen, S., 2023b. Snap: Self-supervised neural maps for visual positioning and semantic understanding. *Advances in Neural Information Processing Systems* 36, 7697–7729.
- Schaer, P., Vallet, J., 2016. Trajectory adjustment of mobile laser scan data in gps denied environments. *The International Archives of the Photogrammetry, Remote Sensing and Spatial Information Sciences* 40, 61–64.
- Schubert, D., Goll, T., Demmel, N., Usenko, V., Stückler, J., Cremers, D., 2018. The tum vi benchmark for evaluating visual-inertial odometry, in: 2018 IEEE/RSJ International Conference on Intelligent Robots and Systems (IROS), IEEE. pp. 1680–1687.
- Schwarz, K.P., El-Sheimy, N., 2004. Mobile mapping systems—state of the art and future trends. *International Archives of Photogrammetry, Remote Sensing and Spatial Information Sciences* 35, 10.
- Shubodh, S., Omama, M., Zaidi, H., Parihar, U.S., Krishna, M., 2024. Liploc: Lidar image pretraining for cross-modal localization, in: Proceedings of the IEEE/CVF Winter Conference on Applications of Computer Vision (WACV) Workshops, pp. 948–957.
- Thalagala, R.G., De Silva, O., Jayasiri, A., Gubbels, A., Mann, G.K., Gosine, R.G., 2024. Mun-fri: A visual-inertial-lidar dataset for aerial autonomous navigation and mapping. *The International Journal of Robotics Research* 43, 1853–1866.
- Tian, Y., Chang, Y., Quang, L., Schang, A., Nieto-Granda, C., How, J.P., Carbone, L., 2023. Resilient and distributed multi-robot visual slam: Datasets, experiments, and lessons learned, in: 2023 IEEE/RSJ International Conference on Intelligent Robots and Systems (IROS), IEEE. pp. 11027–11034.
- Tomešek, J., Čadík, M., Brejcha, J., 2022. Crosslocate: cross-modal large-scale visual geo-localization in natural environments using rendered modalities, in: Proceedings of the IEEE/CVF Winter Conference on Applications of Computer Vision, pp. 3174–3183.
- USGS, U.S.A., 2023. San Francisco B23 LiDAR Data. <https://apps.nationalmap.gov/lidar-explorer/>.
- Uy, M.A., Lee, G.H., 2018. Pointnetvlad: Deep point cloud based retrieval for large-scale place recognition, in: 2018 IEEE/CVF Conference on Computer Vision and Pattern Recognition, pp. 4470–4479. doi:10.1109/CVPR.2018.00470.
- Wang, B., Chen, C., Cui, Z., Qin, J., Lu, C.X., Yu, Z., Zhao, P., Dong, Z., Zhu, F., Trigoni, N., et al., 2021. P2-net: Joint description and detection of local features for pixel and point matching, in: Proceedings of the IEEE/CVF International Conference on Computer Vision, pp. 16004–16013.
- Wang, C., Dai, Y., Elsheimy, N., Wen, C., Retscher, G., Kang, Z., Lingua, A., 2020. Isprs benchmark on multisensory indoor mapping and positioning. *ISPRS Annals of the Photogrammetry, Remote Sensing and Spatial Information Sciences* 5, 117–123.
- Warburg, F., Hauberg, S., Lopez-Antequera, M., Gargallo, P., Kuang, Y., Civera, J., 2020. Mapillary street-level sequences: A dataset for lifelong place recognition, in: Proceedings of the IEEE/CVF conference on computer vision and pattern recognition, pp. 2626–2635.
- Weinmann, M., Jutzi, B., Hinz, S., Mallet, C., 2015. Semantic point cloud interpretation based on optimal neighborhoods, relevant features and efficient classifiers. *ISPRS Journal of Photogrammetry and Remote Sensing* 105, 286–304.
- Wen, W., Zhou, Y., Zhang, G., Fahandezh-Saadi, S., Bai, X., Zhan, W., Tomizuka, M., Hsu, L.T., 2020. Urbanloco: A full sensor suite dataset for mapping and localization in urban scenes, in: 2020 IEEE international conference on robotics and automation (ICRA), IEEE. pp. 2310–2316.
- Wu, H., Zhang, Z., Lin, S., Mu, X., Zhao, Q., Yang, M., Qin, T., 2024. Maplocnet: Coarse-to-fine feature registration for visual re-localization in navigation maps, in: 2024 IEEE/RSJ International Conference on Intelligent Robots and Systems (IROS), IEEE. pp. 13198–13205.
- Xie, Y., Shao, R., Guli, P., Li, B., Wang, L., 2018. Infrastructure based calibration of a multi-camera and multi-lidar system using apriltags, in: 2018 IEEE Intelligent Vehicles Symposium (IV), IEEE. pp. 605–610.
- Ye, J., Lv, Z., Li, W., Yu, J., Yang, H., Zhong, H., He, C., 2024. Cross-view image geo-localization with panorama-bev co-retrieval network, in: European Conference on Computer Vision, Springer. pp. 74–90.
- Yin, J., Li, A., Li, T., Yu, W., Zou, D., 2021. M2dgr: A multi-sensor and multi-scenario slam dataset for ground robots. *IEEE Robotics and Automation Letters* 7, 2266–2273.
- Zhang, C., Zhao, H., Wang, C., Tang, X., Yang, M., 2023. Cross-modal monocular localization in prior lidar maps utilizing semantic consistency, in: 2023 IEEE International Conference on Robotics and Automation (ICRA), IEEE. pp. 4004–4010.
- Zhang, L., Helmberger, M., Fu, L.F.T., Wisth, D., Camurri, M., Scaramuzza, D., Fallon, M., 2022. Hilti-oxford dataset: A millimeter-accurate benchmark for simultaneous localization and mapping. *IEEE Robotics and Automation Letters* 8, 408–415.
- Zhang, X., Zhu, S., Guo, S., Li, J., Liu, H., 2021. Line-based automatic extrinsic calibration of lidar and camera, in: 2021 IEEE International Conference on Robotics and Automation (ICRA), pp. 9347–9353. doi:10.1109/ICRA48506.2021.9561216.
- Zhao, S., Gao, Y., Wu, T., Singh, D., Jiang, R., Sun, H., Sarawata, M., Qiu, Y., Whittaker, W., Higgins, I., et al., 2024. Subt-mrs dataset: Pushing slam towards all-weather environments, in: Proceedings of the IEEE/CVF Conference on Computer Vision and Pattern Recognition,

- pp. 22647–22657.
- Zhao, Z., Yu, H., Lyu, C., Yang, W., Scherer, S., 2023. Attention-enhanced cross-modal localization between spherical images and point clouds. *IEEE Sensors Journal* , 1–1doi:10.1109/JSEN.2023.3306377.
- Zheng, X., Wen, W., Hsu, L.T., 2024. Tightly-coupled visual/inertial/map integration with observability analysis for reliable localization of intelligent vehicles. *IEEE Transactions on Intelligent Vehicles* .
- Zhou, Y., Quang, L., Nieto-Granda, C., Loianno, G., 2024. Coped-advancing multi-robot collaborative perception: A comprehensive dataset in real-world environments. *IEEE Robotics and Automation Letters* .
- Zhu, Y., Kong, Y., Jie, Y., Xu, S., Cheng, H., 2023. Graco: A multimodal dataset for ground and aerial cooperative localization and mapping. *IEEE Robotics and Automation Letters* 8, 966–973. doi:10.1109/LRA.2023.3234802.
- Zou, X., Li, J., Wu, W., Liang, F., Yang, B., Dong, Z., 2025. Reliable-loc: Robust sequential lidar global localization in large-scale street scenes based on verifiable cues. *ISPRS Journal of Photogrammetry and Remote Sensing* 224, 287–301.
- Zuo, X., Geneva, P., Yang, Y., Ye, W., Liu, Y., Huang, G., 2019. Visual-inertial localization with prior lidar map constraints. *IEEE Robotics and Automation Letters* 4, 3394–3401.